

# Interferometric Observation of Cosmic Microwave Background Anisotropies

Martin White<sup>1</sup>, John E Carlstrom<sup>2</sup>, Mark Dragovan<sup>2</sup>, William L Holzapfel<sup>2</sup>

<sup>1</sup>Dept of Astronomy and Dept of Physics,

University of Illinois at Urbana-Champaign, Urbana IL 61801

<sup>2</sup>Dept of Astronomy and Astrophysics,

University of Chicago, Chicago, IL 60637

## ABSTRACT

We present a formalism for analyzing interferometric observations of the Cosmic Microwave Background (CMB) anisotropy and polarization. The formalism is based upon the  $\ell$ -space expansion of the angular power spectrum favored in recent years. Explicit discussions of maximum likelihood analysis, power spectrum reconstruction, parameter estimation, imaging and polarization are given. As an example, several calculations for the Degree Angular Scale Interferometer (DASI) and Cosmic Background Interferometer (CBI) experiments are presented.

*Subject headings:* cosmology:theory – cosmic microwave background

## 1. Introduction

The Cosmic Microwave Background (CMB) has become one of the premier tools for understanding early universe astrophysics, classical cosmology and the formation of large-scale structure. It has a wealth of information about the origin and evolution of the Universe encrypted in its signal. The frequency spectrum is that of a blackbody at 2.73K, confirming the prediction of the standard hot big bang model (see Fixsen et al. 1996, Nordberg & Smoot 1998 or the review of Smoot & Scott 1997). The small angular scale power spectrum of the temperature and polarization anisotropies contain information on the cosmological parameters and the structure that existed at decoupling (see e.g. Bennett, Turner & White 1997).

The predictions for a wide range of cosmological models are now well understood and theoretically secure (Hu et al. 1997; hereafter HSWZ). Experimentally, a flurry of results have been reported in the last five years. The study of the microwave sky has moved beyond the “detection phase” and into the “imaging phase”, with the next generation of experiments planning to provide detailed information about the shape of the angular power spectrum of the temperature anisotropies over a wide range of angular scales.

The advent of low-noise, broadband, millimeter-wave amplifiers (Popieszalski 1993) has made interferometry a particularly attractive technique for detecting and imaging low contrast emission, such as anisotropy in the CMB. An interferometer directly measures the Fourier transform of the intensity distribution on the sky. By inverting the interferometer output, images of the sky are obtained which include angular scales determined by the size and spacing of the individual array elements. In this paper we discuss a formalism for interpreting CMB anisotropies as measured by interferometers and examine what two upcoming experiments, the Degree Angular Scale Interferometer (DASI) and Cosmic Background Interferometer (CBI), may teach us about cosmology.

Several previous papers have dealt with the analysis of CMB data from interferometers (Martin & Partridge 1988; Subrahmanyam et al. 1993; Hobson, Lasenby & Jones 1995; Hobson & Magueijo 1996). In

this paper we extend the work to make explicit contact with the multipole space ( $\ell$ -space) methods now commonly adopted in analyzing single-dish switching experiments, including power spectrum estimation, parameter extraction, imaging, polarization and mosaicing. We also give details of the upcoming DASI experiment.

The outline of the paper is as follows. We begin with a discussion of instruments, past present and future, in §2. Foregrounds and point sources are discussed in §3. The theoretical formalism for analyzing temperature anisotropies is outlined in §4 while applications including maximum likelihood estimation of parameters and power spectrum reconstruction are treated in §5. Increasing the sky coverage, and hence the resolution of the instrument in  $\ell$ -space is introduced in §6. Making images of the microwave sky is addressed in §7. Polarization is treated in §8. Finally, §9 contains our summary and discussion.

## 2. Instruments

The use of interferometers to study fluctuations in the CMB goes back over a decade (see Table 1). Early work using the VLA and ATCA concentrated on small angular scales, reporting a series of upper limits. Recently the CAT (O’Sullivan et al. 1995) has reported a detection of anisotropy on sub-degree scales, at low frequencies (15 GHz). Several groups are now planning to build interferometers which operate at higher frequencies and over a larger range of angular scales, with sensitivities which should enable them to map in detail the CMB anisotropy spectrum from  $\ell \sim 10^2$  to  $\ell \sim 10^3$ .

An interferometric system offers several desirable features: 1) It *directly* measures the power spectrum of the sky, in contrast to the differential or total power measurements. Images of the sky can then be created by aperture synthesis. 2) Interferometers are intrinsically stable since only correlated signals are detected; difficult systematic problems that are inherent in total power and differential measurements are absent in a well designed interferometer. This considerably reduces signals due to ground pickup and near field atmospheric emission. 3) They can be designed for continuous coverage of the CMB power spectrum with angular spectral resolution determined by the number of fields imaged.

Motivated by these attributes, several groups are developing new interferometers targeted at measuring the anisotropy in the CMB on sub-degree angular scales. Three instruments are currently under construction: the Very Small Array (VSA) in Cambridge, the Degree Angular Scale Interferometer (DASI) and the Cosmic microwave Background Interferometer (CBI). DASI and CBI are parallel projects based at Chicago and Caltech. In this paper we will concentrate on the DASI instrument, though the formalism is completely general and applies equally to any interferometer.

DASI is an interferometer designed to measure anisotropies in the CMB over a large range of scales with high sensitivity<sup>1</sup>. The array consists of 13 closely packed elements, each of 20 cm diameter, in a configuration which fills roughly half of the aperture area with a 3-fold symmetry (see Fig. 1). Each element of the array is a wide-angle corrugated horn with a collimating lens. DASI uses cooled HEMT amplifiers running between 26-36 GHz with a noise temperature of  $< 15\text{K}$ . The signal is filtered into ten 1 GHz channels. DASI will operate at the South Pole.

---

<sup>1</sup>More information on DASI can be found at <http://astro.uchicago.edu/dasi>.

Name	Location	$N_{\text{dish}}$	Freq. (GHz)	Bandwidth (GHz)	Primary beam	$\ell$
OVRO <sup>a</sup>	United States	6	30	2.0	4'	6750
VLA <sup>b</sup>	United States	27	8	0.2	5'	6000
Ryle <sup>c</sup>	England	8	15	0.4	6'	4500
BIMA <sup>d</sup>	United States	10	30	0.8	6'	4300
ATCA <sup>e</sup>	Australia	6	9	0.1	8'	3400
T-W <sup>f</sup>	United States	2	43	—	2°	20-100
CAT <sup>g</sup>	England	3	13–17	0.5	2°	339–722
VSA <sup>h</sup>	Canary Islands	15	26–36	2.0	4°	130–1800
DASI <sup>i</sup>	South Pole	13	26–36	10.0	3°	125–700
CBF <sup>j</sup>	Chile	13	26–36	10.0	44'	630–3500

Table 1: Current experiments to measure CMB temperature anisotropies with interferometers. There are published upper limits from VLA, Ryle and ATCA. The CAT has published a detection while VSA, DASI and CBI are expected to begin operations around 1999-2000. The location, number of dishes/horns, frequency and (approximate) coverage in  $\ell$  space are listed.

<sup>a</sup>Carlstrom, Joy & Grego 1996, ApJ, 461, L59

<sup>b</sup>Fomalont EB., et al., 1984, ApJ, 277, L23; Knoke JE., et al., 1984, ApJ, 284, 479; Martin HM. & Partridge RB., 1988, ApJ, 324, 794; Fomalont EB., et al., 1988, Astron J., 96, 1887; Hogan CJ. & Partridge RB., 1989, ApJ, 341, L29; Fomalont EB., et al., 1993, ApJ, 404, 8.; Partridge RB, et al., 1997, ApJ, 483, 38

<sup>c</sup>Jones, ME., 1997, PPEUC proceedings, Cambridge, April 7-11

<sup>d</sup>Cooray, AR. et al. 1997, AAS, 191 1906

<sup>e</sup>Subrahmanyan R., Ekers RD., Sinclair M., Silk J., 1993, MNRAS, 263, 416; Subrahmanyan R., Kesteven MJ., Ekers RD., Silk J., 1998, MNRAS, in press [astro-ph/9805245]

<sup>f</sup>Timbie P.T., Wilkinson D.T., 1990, ApJ, 353, 140

<sup>g</sup>O’Sullivan C., et al., 1995, MNRAS, 274, 861

<sup>h</sup>see Jones, ME., 1996, in Proceedings of the XVIth Moriond Meeting, ed. F. Bouchet et al., p. 161

<sup>i</sup>see Halverson et al., 1998, ASP Conf. Proc., “Astrophysics from Antarctica”, ed. G.Novak & R.Landsberg, in press

<sup>j</sup><http://astro.caltech.edu/~tjp/CBI/>

### 3. Foregrounds

In order to estimate the contribution of primordial fluctuations to the observed signal, it is necessary to estimate the contribution from foreground contaminants. Some reviews of the situation with regards astrophysical foregrounds can be found in Brandt et al. (1994), Toffolatti et al. (1994, 1997) and Tegmark & Efstathiou (1996). We refer the reader to these papers for more details, and lists of references. Below we summarize some of the more important points for the DASI experiment.

### 3.1. Atmosphere

The far field<sup>2</sup> of a very compact array is actually quite near the instrument; for DASI this distance is only a few hundred meters. Thus everything beyond this distance, including the atmosphere, will be imaged by the interferometer. Taking a standard model for the static brightness of the atmosphere with a temperature  $T$  and zenith opacity  $n$ , the brightness varies with zenith distance  $\theta$  as

$$T \left( 1 - \exp \left[ \frac{-n}{\cos(\theta)} \right] \right) \quad . \quad (1)$$

Its effect thus appears as a constant term plus a slope and a very slight curvature. Since the interferometer rejects low spatial frequencies, this atmospheric contribution is negligible in the final image.

The dynamic atmosphere causes a fluctuating brightness we must look through, and if it is in the far field it will be correlated and appear as excess noise (Church 1995). The Python V experiment observed from the South Pole during the austral summer of 1997 at a frequency of 45 GHz and covered angular scales comparable to those of DASI. From the level of atmospheric noise, we estimate that the atmosphere will contribute only about 10% to the total system noise (Lay et al., 1998, in preparation).

### 3.2. Galactic Foregrounds

#### 3.2.1. Synchrotron

Due to its low operating frequency, the main foreground which DASI will need to contend with is Galactic synchrotron radiation, produced by electrons spiraling in the galactic magnetic field. The specific intensity<sup>3</sup> of synchrotron emission roughly follows a power-law in frequency  $I_\nu^{\text{sync}} \propto \nu^\beta$  with spatially varying index and amplitude (Lawson et al. 1987, Banday & Wolfendale 1991, Platania et al. 1998). The index,  $\beta_{\text{sync}}$ , varies from -0.1 to -1.3 with a mean of -0.8. There is some evidence that the index steepens at higher frequencies. The angular power spectrum  $C_\ell \sim \ell^{-3}$  for  $\ell < 10^2$  (see Eq. (6) for a definition of  $C_\ell$ ).

#### 3.2.2. Free-Free

Free-free emission, also known as bremsstrahlung, is due to scattering of unbound particles, typically electrons off nuclei e.g.  $ep \rightarrow ep\gamma$ . The spectral index  $\beta_{\text{ff}}$  depends on the temperature and density of the charged particles, but is in the range -0.13 to -0.16 for typical electron density and temperature values for the ISM (Bennett et al. 1992). At high galactic latitudes, free-free emission is expected to dominate over synchrotron emission at around 40 GHz (Bennett et al. 1992). No direct maps of free-free emission exist, though there is a possible correlation between free-free emission and H $\alpha$  emission (Bennett et al. 1992). Since the H $\alpha$  maps contain striping the significance of the correlation is not easy to assess. If there is a strong correlation the free-free spectrum can be predicted from H $\alpha$  measurements at galactic latitude  $\sim 20^\circ$  (Reynolds 1992) plus fundamental physics to determine  $\beta_{\text{ff}}$ . There is evidence however (Kogut et al. 1996,

---

<sup>2</sup>The farfield distance is  $2B^2/\lambda$  where  $B$  is the longest baseline of the interferometer, 1.1m for DASI, and  $\lambda$  is the wavelength.

<sup>3</sup>To obtain the spectral indices in terms of antenna temperature  $T_A \equiv c^2 I_\nu / (2k\nu^2)$ , or  $\delta T_A = x^2 e^x / (e^x - 1)^2 \delta T$ , one subtracts 2.

Leitch et al. 1997, de Oliveira-Costa et al. 1997, Kogut 1997) that free-free emission may be correlated with dust emission near the NGP, and that this “hot” ( $10^5 - 10^6$ K) component may not emit  $H\alpha$  (for an alternative explanation of the correlation in terms of spinning dust grains, see Draine & Lazarian 1998). A correlation between free-free emission and dust would imply  $C_\ell \sim \ell^{-2.5}$  to  $\ell^{-3}$  (Schlegel et al. 1998, Wright 1998).

### 3.3. Extragalactic Foregrounds

The fluctuations from extragalactic sources have been modeled by Toffolatti et al. (1994, 1997) and Franceschini et al. (1991). The source models are robust below 100 GHz though uncertain to almost an order of magnitude well above 100 GHz.

The angular dependence of uncorrelated point sources is of course that of white noise:  $C_\ell \sim \ell^0$ . There is some evidence that radio sources are correlated (Peacock & Nicholson 1991), but the non-Poisson contribution to the anisotropy is always smaller than the Poisson contribution (Toffolatti et al. 1994, 1997). Providing the sources exist over a large range of distances from us, any correlation in the sources at small scales is significantly diluted by projection.

We show in Fig. 2 the angular power spectrum,  $\ell(\ell + 1)C_\ell \sim \ell^2$ , associated with point sources at 30 GHz, assuming that we subtract all sources brighter than 30mJy. We have taken the luminosity function of VLA FIRST (Becker et al. 1996) radio sources at 1.5 GHz from Tegmark & Efstathiou (1996; Eq. 43) and extrapolated *all* the sources assuming  $I_\nu \sim \nu^{-\alpha}$ . For  $\alpha > 0$  it is below the expected cosmological signal for the range of scales probed by DASI. Point source subtraction for DASI will be facilitated by using the ATCA to map the DASI observing region at 16-26 & 43 GHz (the DASI observing region also overlaps with regions observed by Python and planned observations by Boomerang and Beast).

### 3.4. Foreground Subtraction

We will for definiteness here consider the DASI instrument, though our general conclusions will hold for the other planned instruments with similar frequency coverage. In the absence of external information about foreground emission we can use the 10 GHz bandwidth of DASI to marginalize over the unknown amplitude of a foreground component. Since we are working at low frequency the dominant foregrounds are synchrotron and free-free emission, which have similar spectral indices. Thus one is led to consider fitting out a single component. Using the formalism of Dodelson (1997) and 5 frequency channels centered at 27, 29, 31, 33 and 35 GHz we find that the error bars on the CMB component are increased by a factor of 4.2 (5.1) if we project out a synchrotron (free-free) foreground with (temperature) spectral index -2.7 (-2.2). Using  $10 \times 1$  GHz channels doesn’t change this number significantly. With an improved foreground extraction method it may be possible to reduce this by roughly a factor of 2 (Tegmark 1997a, White 1998).

The increase in the error bar is due to the small operating band of DASI, and indicates that we would like to use external information (foreground maps) when interpreting the DASI observations. As an example, assumptions about the spatial properties of the foregrounds (e.g. their  $\ell$ -space power spectra) can improve the separation of foreground and signal. The DASI will originally operate in a region known to be low in foregrounds, but the need for a large sky coverage will eventually require operation in regions with significant foregrounds. Due to the dependence on the region of sky surveyed, we will focus on the instrument characteristics from now on, and not include the increase in the error bars expected from

foreground subtraction.

## 4. Formalism

### 4.1. The Visibility

An interferometer measures  $\langle E_1 E_2^* \rangle$  where  $E_1$  and  $E_2$  are the electric field vectors measured by two telescopes pointing to the same position on the sky and  $\langle \dots \rangle$  represents an average over a time long compared with the period of the wave. Assuming for now a monochromatic source of radiation and working in the Fraunhofer limit, the average of the product of electric fields is the intensity times a phase factor. For each point source, the phase factor is the exponential of ( $i$  times) the geometric path difference between the source and the two telescopes, in units of the wavelength. Taking the integral over the source/emitter plane gives the Fourier Transform of the observed intensity (i.e. the sky intensity multiplied by the instrument beam).

The fundamental observable for the interferometer is thus a “visibility”, which is the Fourier Transform (FT) of the sky intensity multiplied by the primary beam or aperture function (Tompson, Moran & Swenson 1986):

$$V(\vec{u}) \propto \int d\hat{x} A(\hat{x}) \Delta T(\hat{x}) e^{2\pi i \vec{u} \cdot \hat{x}} \quad (2)$$

where  $\Delta T$  is the temperature (fluctuation) on the sky,  $\hat{x}$  is a unit 3-vector and  $\vec{u}$  is the conjugate variable, with dimensions of inverse angle measured in wavelengths.  $A(\hat{x})$  is the “primary” beam and is typically normalized to unity at peak, which is  $\sqrt{2\pi}\sigma$  larger than the usual normalization of a gaussian beam. (By requiring  $A(0) = 1$  we ensure that the area of the aperture in the  $\vec{u}$  plane is unity.) The spacing of the horns and the position of the beam on the sky determine which value of  $\vec{u}$  will be measured by a pair of antennae in any one integration. The size of the primary beam determines the amount of sky that is viewed, and hence the size of the “map”, while the maximum spacing determines the resolution.

Typically the field of view of the interferometer is small, so in what follows we will make a small angle approximation and treat the sky as flat (see also the Appendix). This is a very good approximation for the upcoming experiments (CBI, DASI, VSA) and leads to significant simplification in the formalism. If the primary beam  $A(\hat{x})$ , or more generally the area of sky surveyed, is well localized the integral is only over a very small range of  $\hat{x}$ . Denoting the center of the beam by  $\hat{x}_0$  we can write  $\hat{x} = \hat{x}_0 + \mathbf{x}_\perp$  with  $x_\perp \ll x_0 = 1$  and  $\mathbf{x}_\perp \cdot \hat{x}_0 = 0$ , then  $\mathbf{x}_\perp$  is a 2D vector lying in the plane of the sky. We will denote 2D vectors by boldface type, and vectors in 3D or other spaces by arrows. A vector name which is neither boldface nor arrowed indicates the length of that vector, e.g.  $x_\perp = |\mathbf{x}_\perp|$ .

Finally we should remark on one subtlety in the statistical analysis of a “random” component such as the CMB fluctuations. It is common to assume that the temperature fluctuations in the CMB are realizations of a random field, so that  $T(\mathbf{x})$  is a real random field on  $R^2$  (see below). Since  $V(\vec{u})$  is the Fourier Transform of  $T(\mathbf{x})$ , it is also a random field, however it is complex. Since  $T$  is real, it follows that  $V^*(\vec{u}) = V(-\vec{u})$  and thus  $V(\vec{u})$  is a complex random field with independent degrees of freedom only over the half-plane (i.e. twice as many as  $T$  over half the area). This restriction to the half-plane will be important when it comes to parameter estimation. An alternate formulation of the problem, which turns out to be equivalent, is to define a “real” visibility in terms of cosine (sine) transforms whenever e.g.  $u_x > 0$  ( $u_x < 0$ ). We will not give this parallel development here, as it is exactly equivalent to the complex case we will discuss.

## 4.2. The Sky Power Spectrum

To proceed, notice that in the small field of view approximation the visibility is the convolution of the FT of the sky intensity (temperature) and the FT of the primary beam. Thus if we knew the power spectrum of the sky, we could find the power spectrum of the visibilities by convolution with the Fourier transform of the primary beam (see below). In this section we will concentrate on the sky power spectrum and neglect the effect of the primary beam, and so we set  $A = 1$  for now.

We usually assume that our theory has no preferred direction, i.e. it is rotationally invariant. In the flat sky approximation this rotational invariance becomes a translational invariance on the plane. This means that the (double) FT of the sky correlation function becomes diagonal in  $\mathbf{u}$ , i.e. “conserves momentum”. (We discuss the flat sky approximation further in the Appendix.) We shall call the diagonal part the sky power spectrum  $S(\mathbf{u}) = S(u)$ , not to be confused with a flux.

The ability to perform Fourier analysis on the “flat” sky and the replacement of rotational by translational invariance is the principle advantage of the flat sky approximation. These advantages are *only* obtained in the small-angle limit, regardless of how one chooses to map angle into  $u$ , so the reader should beware of “improvements” to the flat sky approximation except under very special circumstances.

We can write the FT of the correlation function, depending on  $\mathbf{u}$  and  $\mathbf{w}$ , as

$$\int d\mathbf{x}_1 d\mathbf{x}_2 C(\mathbf{x}_1 \cdot \mathbf{x}_2) \exp[2\pi i \mathbf{u} \cdot (\mathbf{x}_1 - \mathbf{x}_2)] \exp[2\pi i (\mathbf{w} - \mathbf{u}) \cdot \mathbf{x}_1] \quad , \quad (3)$$

where  $C(\cos \theta)$  is the (dimensionless) correlation function for the CMB temperature fluctuations, defined below. If we expand

$$e^{2\pi i \mathbf{u} \cdot \mathbf{x}} = J_0(2\pi u) + 2 \sum_{m=1}^{\infty} i^m J_m(2\pi u) \cos(m \arccos(\hat{u} \cdot \hat{x})) \quad (4)$$

and use the symmetry of the problem to do the angular integrals we find (e.g. Subrahmanyam et al. 1993) that the diagonal part

$$S(u) \propto \int_0^2 \omega d\omega C(\omega) J_0(2\pi u \omega) \quad (5)$$

where  $\omega = |\mathbf{x}_1 - \mathbf{x}_2| = 2 \sin(\theta/2)$  and  $d(\cos \theta) = \omega d\omega$ . In the flat space limit we extend the upper limit of the  $\omega$  integration to  $\infty$ . Expanding the correlation (or 2-point) function for the CMB temperature fluctuations as a Legendre series

$$C(\mathbf{x}_1 \cdot \mathbf{x}_2) \equiv \left\langle \frac{\Delta T}{T}(\mathbf{x}_1) \frac{\Delta T}{T}(\mathbf{x}_2) \right\rangle = \frac{1}{4\pi} \sum_{\ell=2}^{\infty} (2\ell + 1) C_\ell P_\ell(\mathbf{x}_1 \cdot \mathbf{x}_2) \quad (6)$$

and using Gradshteyn & Ryzhik (1980; Eq. 7.251(3)) we obtain

$$S(u) = \frac{1}{2\pi u} \sum_{\ell} (2\ell + 1) C_\ell J_{2\ell+1}(4\pi u). \quad (7)$$

In evaluating this sum, care must be taken for regions of the spectrum where  $C_\ell$  is nearly scale invariant due to significant cancellations.

For large  $\ell$ ,  $J_{2\ell+1}$  is a sharply peaked function. Thus the 2D power spectrum  $u^2 S(u) \sim \ell(\ell + 1) C_\ell|_{\ell=2\pi u}$ . Direct numerical evaluation of Eq. (7) or requiring the RMS fluctuation at zero lag to be the same in  $u$  space

as  $\ell$  space (Gradshteyn & Ryzhik 1980, Eq. 6.511(1)) allows us to write

$$u^2 S(u) \simeq \frac{\ell(\ell+1)}{(2\pi)^2} C_\ell \Big|_{\ell=2\pi u} \quad \text{for } u \gtrsim 10 \quad . \quad (8)$$

This approximation works at the few percent level for standard CDM (sCDM) when  $u \gtrsim 10$  or  $\ell \gtrsim 60$ .

We show  $S(u)$  vs.  $u$  for a selection of CDM models normalized to the *COBE* 4-year data in Fig. 3. The range of angular scales that will be probed by DASI and CBI are shown as the solid lines across the top of the figure. While these models were chosen primarily to fit the large-scale structure data, all of the models shown provide reasonable fits to the current CMB data. The parameters for the models are given in Table 2.

### 4.3. The Visibility Correlation Matrix

In theories which predict gaussian temperature fluctuations the fundamental theoretical construct is the correlation matrix of the measured data. Since the data in our case are the visibilities measured at a set of points  $\mathbf{u}_i$ , in what follows we will need to know the correlation matrices for the signal and noise in the various visibilities. The measured fluxes,  $V(\mathbf{u})$ , are

$$V(\mathbf{u}) = \frac{\partial B_\nu}{\partial T} T_{\text{CMB}} \int d\mathbf{x} \frac{\Delta T(\mathbf{x})}{T_{\text{CMB}}} A(\mathbf{x}) e^{2\pi i \mathbf{u} \cdot \mathbf{x}} \quad (9)$$

where  $\partial B_\nu / \partial T$  converts from temperature to intensity,  $T_{\text{CMB}}$  is the CMB temperature and  $A(\mathbf{x})$  is the primary beam. The conversion factor from “temperature” to “intensity” is

$$\frac{\partial B_\nu}{\partial T} = \frac{2k_B}{c^2} \left( \frac{k_B T}{h} \right)^2 \frac{x^4 e^x}{(e^x - 1)^2} \simeq \left( \frac{99.27 \text{ Jy sr}^{-1}}{\mu \text{ K}} \right) \frac{x^4 e^x}{(e^x - 1)^2} \quad (10)$$

where  $B_\nu$  is the Planck function,  $k_B$  is Boltzman’s constant,  $x \equiv h\nu/k_B T_{\text{CMB}} \simeq \nu/56.84 \text{ GHz}$  is the “dimensionless frequency” and  $1 \text{ Jy} = 10^{-26} \text{ W/m}^2/\text{Hz}$ . In the Rayleigh-Jeans limit  $\partial B_\nu / \partial T \simeq 2k_B(\nu/c)^2$  where  $\nu$  is the observing frequency. This is a good approximation for the frequencies of planned interferometers, the correction to the Rayleigh-Jeans assumption is 2% at 30 GHz, and we shall make it henceforth. We shall also set  $c \equiv 1$  so  $\nu = \lambda^{-1}$ .

The Fourier Transform of the primary beam<sup>4</sup> is the auto-correlation of the Fourier Transform of the point response,  $g$ , of the receiver to an electric field,  $\tilde{A}(u) = \tilde{g} \star \tilde{g}(u)$  and

$$A(\mathbf{x}) = \int d\mathbf{u} \tilde{A}(\mathbf{u}) e^{-2\pi i \mathbf{u} \cdot \mathbf{x}} \quad , \quad (11)$$

so using the fact that the power spectrum is diagonal in  $\mathbf{u}$  we have

$$C_{ij}^V \equiv \langle V^*(\mathbf{u}_i) V(\mathbf{u}_j) \rangle = (2k_B T_{\text{CMB}} \nu^2)^2 \int d^2 w \tilde{A}^*(\mathbf{u}_i - \mathbf{w}) \tilde{A}(\mathbf{u}_j - \mathbf{w}) S(|\mathbf{w}|) \quad . \quad (12)$$

Notice that the visibilities are uncorrelated if  $|\mathbf{u}_i - \mathbf{u}_j|$  is larger than (twice) the width of  $\tilde{A}$ , which defines the bin size  $\Delta u$ .

---

<sup>4</sup>Throughout we will use a tilde to represent the Fourier Transform of a quantity.



We are now in a position to define the window function  $W_{ij}(u)$  which, when convolved with the power spectrum, defines the visibility correlation matrix  $C_{ij}^V$ . From the above

$$C_{ij}^V = (2k_B T_{\text{CMB}} \nu^2)^2 \int_0^\infty w dw S(w) W_{ij}(w) \quad (13)$$

with

$$W_{ij}(|\mathbf{w}|) \equiv \int_0^{2\pi} d\theta_w \tilde{A}^*(\mathbf{u}_i - \mathbf{w}) \tilde{A}(\mathbf{u}_j - \mathbf{w}) \quad . \quad (14)$$

Note that since  $\tilde{A}$  has compact support the maximum of  $W_{ii}$  scales as  $u_i^{-1}$  for  $u_i \gg \Delta u$ . Since the noise per visibility is independent of  $u_i$  the signal-to-noise drops as  $u^{-2}$  for a scale-invariant spectrum,  $S(u) \propto u^{-2}$ . Also note that both  $W_{ij}$  and  $S(u)$  are positive semi-definite, so the visibilities are never anti-correlated, unlike single-dish (chopping) experiments.

In general the distribution of the electric field in the horn aperture is close to a pillbox times a Gaussian. Due to the finite aperture  $\tilde{A}$  has compact support. Usually the response is independent of  $\hat{u}$ : we will call the  $|\mathbf{u}|$  for which  $\tilde{A}$  vanishes  $\Delta u$ . In order to obtain a simple estimate of our window function it is a reasonable first approximation to take  $\tilde{A}$  equal to the auto-correlation of a pillbox of radius  $D/2$  where  $D$  is the diameter of the dish. Specifically

$$\tilde{A}(\mathbf{u}) = \frac{2\tilde{A}_*}{\pi} \left[ \arccos \frac{u}{D} - \frac{u\sqrt{D^2 - u^2}}{D^2} \right] \quad (15)$$

if  $u \leq D$  and zero otherwise. Thus in this simple example  $\Delta u = D$ . If we require  $A(0) = 1$  then this must integrate to unit area, so  $\tilde{A}_*^{-1} = \pi(D/2)^2$ , or the area of the dish.

In the case where all correlated signal is celestial, the correlation function of the noise is diagonal with

$$C_{ij}^N = \left( \frac{2k_B T_{\text{sys}}}{\eta_A A_D} \right)^2 \frac{1}{\Delta_\nu t_a n_b} \delta_{ij} \quad . \quad (16)$$

Here  $T_{\text{sys}}$  is the system noise temperature,  $\lambda$  the wavelength,  $\eta_A$  is the aperture efficiency,  $A_D$  is the physical area of a dish (not to be confused with  $A(\mathbf{x})$ ),  $n_b$  is the number of baselines<sup>5</sup> corresponding to a given separation of antennae,  $\Delta_\nu$  is the bandwidth and  $t_a$  is the observing time. Typical values for DASI are  $T_{\text{sys}} = 20\text{K}$ ,  $\eta_A \sim 0.8$ , dishes of diameter 20 cm,  $n_b = 3$  and  $\Delta_\nu = 10$  GHz (in  $10 \times 1$  GHz channels). For CBI the dishes are 5 times larger with the other numbers about the same. We show in Fig. 4 the diagonal entries of  $C^V$  and  $C^N$  for one pointing and 1 day of observing with DASI.

Using Eqs. (12, 16) we can provide a rough estimate of the signal-to-noise expected in a given visibility. For  $\tilde{A}$  given by Eq. (15) we have

$$\frac{C_{ii}^V}{C_{ii}^N} \sim \left( \frac{T_{\text{CMB}}}{T_{\text{sys}}} \right)^2 \Delta_\nu t_a n_b \left( \frac{\Delta u}{u} \right)^2 u^2 S(u) \quad (17)$$

which given the numbers above yields  $C_{ii}^V/C_{ii}^N \sim 10^3 (\Delta u/u)^2$  for 1 day of integration, assuming a COBE normalized, scale-invariant spectrum.

---

<sup>5</sup>The number of baselines formed by  $n_r$  receivers is  $n_b = n_r(n_r - 1)/2$ .

## 5. Comparison with Theory

### 5.1. Likelihood function

In stochastic theories  $\Delta T(\hat{x})$  is a (gaussian) random variable with zero mean and dispersion given by the  $C_\ell$ . Thus the visibilities measured by the interferometer will be gaussian random variables with zero mean and dispersion  $C^V + C^N$ . For a given set of measured visibilities one can test any theory, or set of  $\{C_\ell\}$ , by constructing the likelihood function (for complex variables  $V$ )

$$\mathcal{L}(\{C_\ell\}) = \frac{1}{\pi^n \det C} \exp[-V^*(\mathbf{u}_i)C_{ij}^{-1}V(\mathbf{u}_j)] \quad (18)$$

where  $C_{ij} = C_{ij}^V + C_{ij}^N$  is the correlation matrix of visibilities at  $\mathbf{u}_i$  and  $\mathbf{u}_j$  (Hobson, Lasenby & Jones 1995). Note that the visibilities are complex and thus the likelihood function is slightly different than for the case of real gaussian random variables, e.g. the “missing” factor of  $\frac{1}{2}$  in the exponent. The restriction to the half-plane however ensures that the number of degrees of freedom is the same as for the real case (c.f. Hobson, Lasenby & Jones 1995).

Name	$\Omega_{\text{mat}}$	$h$	$\Omega_{\text{B}}h^2$	$n$
sCDM	1	0.5	0.0125	1
OCDM	0.5	0.6	0.0200	1
tCDM	1	0.5	0.0250	0.8

Table 2: The cosmological parameters for the theories discussed in the text. All models have  $\Omega_\Lambda = 0$  and have been normalized to the *COBE* DMR 4-year data.

Given a set of data  $\{V_i\}$  one can proceed to test theories using the likelihood function. Confidence intervals for parameters and relative likelihood of theories are calculated in the usual way.

### 5.2. Power Spectrum Estimation

There are several ways one could consider estimating the angular power spectrum from a set of visibilities. Conceptually the simplest is to average  $|V(\vec{u})|^2$  in shells of constant  $|\vec{u}|$ . This gives a (noised biased) estimate  $C_\ell$  at  $\ell = 2\pi u$ , convolved with the window function  $W_{ij}$ .

A more sophisticated method is to define as a “theory” a set of bandpowers, i.e. define the power spectrum  $\ell(\ell+1)C_\ell$  as a piecewise constant, in  $N_{\text{band}}$  bands  $B$ . One then maximizes the likelihood function for this “theory”, the result is the best fitting power spectrum, binned into groups at similar  $\ell$ . Such an approach has been used on the *COBE* 4-year data by Gorski (1996) and Bunn & White (1996), and discussed extensively by Bond, Jaffe & Knox (1998). It is the method we shall advocate here.

As pointed out by Bond, Jaffe & Knox (1998), it is particularly simple to find the maximum of the likelihood function for such a “theory” using a quadratic estimator (see also Tegmark 1997b) which takes as an input a trial theory. In this case the theory is a set of “bandpowers” chosen to cover the  $\ell$  range of interest and be approximately independent. Iteration of the quadratic estimator is equivalent to Newton’s method for finding the root of  $d\mathcal{L}/dp$  where  $p$  is a parameter on which  $\mathcal{L}$  depends.

Specifically from an estimate of the bandpowers,  $u^2 S(u) = \hat{p}_\alpha$  for  $u \in B_\alpha$  (where  $\alpha = 1, \dots, N_{\text{band}}$ ) an improved estimate is  $p_\alpha = \hat{p}_\alpha + \delta p_\alpha$  with

$$\delta p_\alpha = \left( \text{tr} \left[ \hat{C}^{-1} \hat{C}_{,\alpha} \hat{C}^{-1} \hat{C}_{,\beta} \right] \right)^{-1} \text{tr} \left[ (C - \hat{C}) \left( \hat{C}^{-1} \hat{C}_{,\beta} \hat{C}^{-1} \right) \right] \quad (19)$$

(Bond, Jaffe & Knox 1998). Here  $\hat{C}$  indicates the (theoretical) correlation matrix evaluated at the initial estimate  $\hat{p}_\alpha$  with  $C_{,\alpha} \equiv dC/dp_\alpha$  and  $C \equiv V^*(\mathbf{u}_i)V(\mathbf{u}_j)$  indicates the matrix formed by the data. Iteration of this procedure (e.g. from an initially flat spectrum  $p_\alpha = \text{constant}$ ) converges to the maximum likelihood estimate of the power spectrum.

Since the parameters  $p_\alpha$  are chosen to be the (constant) values of  $u^2 S(u)$  across the band  $B_\alpha$  and the noise is assumed to be independent of the level of cosmological signal

$$\left[ \hat{C}_{,\alpha} \right]_{ij} = (2k_B T_{\text{CMB}} \nu^2)^2 \int_{B_\alpha} \frac{dw}{w} W_{ij}(w) \quad . \quad (20)$$

We may gain some intuition for this expression by considering the simple case of 1 band and uncorrelated visibilities. Assume additionally that  $W_{ij}(\mathbf{u})$  is independent of  $\hat{u}$ . Then if we write  $\hat{C} = \sigma_i^2 w_i \delta_{ij}$  and  $\hat{C}_{,\alpha} = w_i \delta_{ij}$  we have

$$\delta p_\alpha = \left( \sum_i \sigma_i^{-4} \right)^{-1} \sum_j \frac{|V_j|^2 w_j^{-1} - \sigma_j^2}{\sigma_j^4} \quad . \quad (21)$$

This becomes even simpler if all of the visibilities are at fixed  $|\mathbf{u}_i|$ . Then  $\sigma_i^V$  is independent of  $i$  and, if we assume the noise is also,  $\delta p$  becomes zero when

$$(\sigma^V)^2 = \frac{1}{N} \sum_{j=1}^N |V_j|^2 w_j^{-1} - (\sigma^N)^2 \quad (22)$$

which is reminiscent of our simplistic estimate described at the beginning of this section.

### 5.3. CDM Parameter Estimation

It has become common (Scott & White 1995, Jungman et al. 1996, Bond, Efstathiou & Tegmark 1997, Zaldarriaga et al. 1997, Stompor & Efstathiou 1998) to ask how well we could measure theory parameters “on average” given a set of measurements  $\{V_i\}$  which are “typical”. Imagine that our theory is defined by a set of parameters  $\{p_\alpha\}$  and that the sky corresponds to this theory with values of parameters  $\hat{p}_\alpha$ . In this case

$$\langle -\ln \mathcal{L} \rangle = \text{tr} \left[ \hat{C} C^{-1} + \ln C \right] \quad (23)$$

where  $\hat{C}_{ij} = \langle V_i^* V_j \rangle$  denotes  $C_{ij}(\hat{p})$ . The precision to which we can measure  $\{p_\alpha\}$  assuming an input theory  $\hat{C}$  is given by the second derivative matrix of  $\langle -\ln \mathcal{L} \rangle$

$$\left. \frac{\partial^2 \langle -\ln \mathcal{L} \rangle}{\partial p_\alpha \partial p_\beta} \right|_{\hat{p}} = \text{tr} \left[ \hat{C}^{-1} \hat{C}_{,\alpha} \hat{C}^{-1} \hat{C}_{,\beta} \right] \quad (24)$$

with  $C_{,\alpha} \equiv dC/dp_\alpha$ . Thus

$$\langle (p_\alpha - \langle p_\alpha \rangle)(p_\beta - \langle p_\beta \rangle) \rangle_{\mathcal{L}} = \left\{ \text{tr} \left[ \hat{C}^{-1} \hat{C}_{,\alpha} \hat{C}^{-1} \hat{C}_{,\beta} \right] \right\}^{-1} \quad (25)$$

where  $\langle \dots \rangle_{\mathcal{L}}$  denotes an average with respect to the likelihood function  $\mathcal{L}$ .

As an example of how well planned interferometers will constrain cosmological models we can ask how well DASI would be able to determine the cosmological parameters  $p_\alpha = \{C_{10}, \Omega_{\text{mat}}, h, \Omega_B h^2, n\}$  for the adiabatic CDM models listed in Table 2. We have not included the ionization history in this list since the amplitude and the ionization history are degenerate on these scales for late reionization. We will also assume that  $\Omega_\Lambda = 0$ . We choose the value of  $C_\ell$  at  $\ell = 10$  for our normalization parameter as this is approximately the “pivot point” of the *COBE* data.

In order to avoid a detailed modeling of the DASI observing strategy before the instrument is operational, we shall simply assume that DASI will fully sample the  $u-v$  half-plane between  $u = 25$  and 110. The number of different  $\hat{u}$  needed to cover the  $u-v$  ring at  $u$  if the aperture has a radial width  $2\Delta u$  is  $N(u) = 2u/\Delta u$ , where we have made use of the fact that only the *half*-plane is covered. (This is actually conservative – points do not become correlated as soon as the  $\tilde{A}$ ’s touch. We would want to sample a factor of  $\sim 2$  more densely than this and keep track of correlations, but we shall postpone an optimization to a later paper). The DASI has continuous sensitivity in  $|\mathbf{u}|$ . Thus we assume that we can fully cover the  $u-v$  plane with  $N(u_{\text{max}})$  pointings (orientations) of the instrument. We spend equal time on each orientation.

To simplify this computation we will count only the *independent* visibility measurements arising from such a strategy, i.e. ignore the extra information that will be available from the correlations. Specifically we choose  $\mathbf{u}_i$  such that there are  $N_{\text{bin}}$  independent bins in the radial ( $|\mathbf{u}|$ ) direction and  $N(|\mathbf{u}_i|)$  bins in the angular ( $\hat{u}$ ) direction. Eq. (25) in the case that  $C_{ij}$  is diagonal reduces simply to

$$\langle (p_\alpha - \langle p_\alpha \rangle)(p_\beta - \langle p_\beta \rangle) \rangle_{\mathcal{L}}^{-1} = \sum_{i=1}^{N_{\text{bin}}} N(|\mathbf{u}_i|) \frac{\hat{C}_{ii,\alpha}^V \hat{C}_{ii,\beta}^V}{(\hat{C}_{ii}^V + \hat{C}_{ii}^N)^2} \quad (26)$$

where we have assumed the noise is independent of  $p_\alpha$ . The width of the aperture  $\Delta u$  is chosen so that  $u_{\text{max}} - u_{\text{min}} = 2N_{\text{bin}}\Delta u$ . To obtain this resolution in  $u$  requires increasing the sky coverage either by shrinking the dish size or by mosaicing (see §6). We shall assume that if mosaicing is used then the spherical symmetry of  $\tilde{A}$  is preserved. As discussed in §6, this will only be an approximation. A full analysis of the strategy including mosaicing, which takes into account the deviations from the monochromatic and “flat sky” approximations and includes the correlations between visibilities remains to be done. The number of bins is used here as a measure of the sky coverage achieved by the experiment. For reference  $N_{\text{bin}} = 20$  corresponds to a  $10^3$  square degree circle of sky.

We shown in Table 3 the relative uncertainties on  $p_\alpha$ , with a “prior” 20% uncertainty in  $C_{10}$ . (We do not include the increase in the errors from foreground subtraction here.) The number of bins is fixed at  $N_{\text{bin}} = 20$ , or  $10^3$  square degrees of sky coverage, for simplicity. For 3 months of observing an sCDM sky the DASI would be system noise limited for  $u \gtrsim 50$ . Note that there is a strong dependence of the estimated errors on the input theory (and the parameter set chosen). We have chosen the 3 theories here to explore this dependence. For the open model (which has  $\Omega_0 = 0.5$ ) the peaks in the power spectrum are at higher  $u$  than the critical density models (see Fig. 3). This means that there is less information (from the higher peaks) available to break the degeneracy in parameter variations, leading to larger uncertainties when the other parameters are integrated out. To increase the precision with which cosmological parameters could be determined in an open model, one would need to extend the coverage to higher  $|\mathbf{u}|$  using CBI. If this is done the angular scale of the features in the open model is better matched to DASI+CBI than in the flat models, and the parameters can thus be better determined. For the tilted model the signal-to-noise is lower at large  $u$ , which accounts for the slightly larger uncertainties on e.g. the spectral slope  $n$ . However the

higher baryon fraction leads to greater sensitivity to  $\Omega_B$ , and the variations with  $\Omega_{\text{mat}}$  are less correlated with  $\Omega_B$ .

Name	3 months				6 months				12 months			
	$\Omega_{\text{mat}}$	$h$	$\Omega_B$	$n$	$\Omega_{\text{mat}}$	$h$	$\Omega_B$	$n$	$\Omega_{\text{mat}}$	$h$	$\Omega_B$	$n$
sCDM	21	40	50	9	15	26	34	7	12	19	27	5
OCDM	–	–	–	62	73	–	–	45	53	–	91	33
tCDM	30	71	40	16	17	39	25	10	11	23	17	7

Table 3: The *percentage* relative uncertainties for the cosmological parameters assuming 3, 6 or 12 months of integration of the DASI over  $10^3$  square degrees ( $N_{\text{bin}} = 20$ ), for the theories discussed in the text. We have included a “prior” corresponding to 20% uncertainty in  $C_{10}$ . For the open models several parameters are very correlated because DASI alone does not probe to high enough  $u$ . For sCDM with  $N_{\text{bin}} = 20$  and  $T_{\text{sys}} = 20\text{K}$  we are noise limited for  $u \gtrsim 50$  with 3 months observing time. Once DASI and CBI are combined the uncertainties on all parameters for all models are  $< 20\%$  for 1 year of data.

For all of these theories the uncertainties are larger due to the large correlations between parameters: if the bin size or noise is too large then one cannot distinguish between variations in different parameters, inflating the marginalized errors. To decrease the correlations one must increase the resolution in  $u$ , which means obtaining more sky coverage, or increase the total range of  $u$  covered, which means combining DASI and CBI. The combination of DASI and CBI is particularly powerful, with the marginalized errors for each model being below 20% for all parameters within 1 year of observing.

## 6. Mosaicing

### 6.1. Increasing Resolution

The resolution which we have in  $u$ -space is limited by the amount of sky that we have surveyed, which for a single pointing is equal to the size of the primary beam. By combining several contiguous pointings of the telescope we can increase the amount of surveyed sky and therefore increase the resolution in  $u$ -space. This is known as mosaicing. The idea here is to measure the visibility as a function of position  $\mathbf{y}$  from the map or phase center

$$V_{\mathbf{y}}(\mathbf{u}) \propto \int d^2x A(\mathbf{x} - \mathbf{y})T(\mathbf{x})e^{2\pi i\mathbf{u}\cdot\mathbf{x}} \quad (27)$$

We then sample  $V_{\mathbf{y}}$  at a series of points by repointing the entire telescope. Let us denote this by a sampling function  $\Pi(\mathbf{y})$  which will be a sum of delta functions. We compute the Fourier Transform of  $\Pi(\mathbf{y})V_{\mathbf{y}}$  which is simply the convolution  $\{\tilde{\Pi} \star \tilde{V}\}(\mathbf{v})$  where

$$\tilde{V}(\mathbf{u}, \mathbf{v}) = \tilde{A}(\mathbf{v})\tilde{T}(\mathbf{u} + \mathbf{v}) \quad . \quad (28)$$

Here  $\mathbf{u}$  is the original vector in the  $u - v$  plane, and  $\mathbf{v}$  is the variable conjugate to  $\mathbf{y}$ .

If our sampling function is a sum of delta functions then  $\tilde{\Pi}$  is a sum of plane waves. Thus simply summing our  $V_{\mathbf{y}}$  at points  $\mathbf{y}_j$  with weight  $c_j$  changes our aperture in  $u$ -space from  $\tilde{A}$  to

$$\sum_j c_j e^{-2\pi i\mathbf{v}\cdot\mathbf{y}_j} \tilde{A}(\mathbf{v}) \quad (29)$$

which can be made much narrower. This is completely analogous to the usual case of Fraunhofer diffraction through many holes, treated in most textbooks on optics. The simplest example is when  $c_j = 1$  and the  $\mathbf{y}_j$  lie on a regular  $N \times N$  grid with spacing  $\delta$  then

$$\sum_j e^{-2\pi i \mathbf{v} \cdot \mathbf{y}_j} = \exp \left[ -2\pi i \mathbf{v} \cdot \delta \frac{(N-1)}{2} \right] \frac{\sin [N2\pi v_x \delta_x]}{\sin [2\pi v_x \delta_x]} \frac{\sin [N2\pi v_y \delta_y]}{\sin [2\pi v_y \delta_y]} . \quad (30)$$

The second diffraction spike occurs at  $v_{x,y} = \delta_{x,y}^{-1}$ . If we choose  $\delta_{x,y}$  sufficiently small (Nyquist sampling) then this will be outside the range where  $\tilde{A}$  vanishes<sup>6</sup>. Fig. 5 shows the gain for a  $3 \times 3$  mosaic.

In the absence of a preferred direction in the theory, the power spectrum of the sky is symmetric in  $\hat{u}$ , so choosing a mosaicing strategy based on a cartesian grid is not optimal. We would like to have the mosaicing maximally rotationally symmetric within the observing constraints. In Fig. 5 we compare the  $3 \times 3$  square to 7 points laid out at the center and vertices of a regular hexagon, with all points equidistant from their neighbors.

Note that mosaicing does not increase the *range* of  $u$  to which we are sensitive (see Eq. 28), it simply enhances our *resolution* by allowing us to follow more periods of a given wave. Thus we retain our ability to reject long-period noise or foregrounds.

If the goal were simply a measurement of the power spectrum, it is just as efficient to use smaller telescopes (with intrinsically better  $u$  resolution) and integrate for longer as it is to use large dishes and mosaic to increase the resolution. The advantage of the later method is that it allows better imaging of each piece of sky for checks of systematics, non-gaussian features and foregrounds and it is easier to avoid “dropouts” in the  $u$  coverage for the power spectrum.

There are two routes to analyzing mosaiced data. The first is to treat the visibilities  $V_{\mathbf{y}_j}(\mathbf{u}_i)$  as separate data, highly correlated in a calculable way, with apparently low resolution but much information in the correlations between visibilities. The theory correlation matrix of mosaiced data can be written in the form of Eq. (13) with a modified window function which allows different pointing centers for each visibility

$$W_{ij}(|\mathbf{w}|) \equiv \int_0^{2\pi} d\theta_w \tilde{A}^*(\mathbf{u}_i - \mathbf{w}) \tilde{A}(\mathbf{u}_j - \mathbf{w}) e^{2\pi i[(\mathbf{u}_j - \mathbf{w}) \cdot \mathbf{y}_j - (\mathbf{u}_i - \mathbf{w}) \cdot \mathbf{y}_i]} . \quad (31)$$

We discuss this further in §6.2 below.

The other route is to statistically weight the  $V(\mathbf{u}_i)$  from the different  $\mathbf{y}_j$  to form a synthesized data set with fewer visibilities and correlations and intrinsically higher resolution. This method is perhaps simpler to understand but the weighting of the different  $\mathbf{y}_j$  will probably not be optimal for parameter estimation or power spectrum estimation.

## 6.2. Optimal Subspace Filtering

A set of data from several (mosaiced) pointings involves many measured visibilities, very few of which are independent. Thus likelihood analysis requires repeated inversion of a large matrix, which can be computationally quite slow. One method for increasing the efficiency of the calculation is to work with a

---

<sup>6</sup>If we sample at precisely the spatial Nyquist rate, gain variations from stare to stare will also alias power outside of the spatial frequency window.

subset of the data which contains most of the signal, but has fewer elements. This transformation can be accomplished using an “optimal subspace filter”.

Consider first the case of a single (unmosaiced) pointing. For the *DASI* the visibilities will be measured at a specified set of  $\mathbf{u}$  at any one time, and then the instrument will be rotated about an axis through the center of the aperture plane to obtain a different set of  $\mathbf{u}$  with the same lengths but different orientations. In this way most of the  $u - v$  plane will be covered allowing for imaging. The number of rotations will be chosen to almost fully sample the  $u - v$  plane at the highest resolution (largest baseline or largest  $u$ ). This means that considerable oversampling of the smaller baselines must result, since the aperture  $\tilde{A}$  has a fixed width  $\Delta u$ . Phrased another way, the correlation matrix  $C_{ij}^V$  of our visibilities has dimension  $\sim (u_{\max}/\Delta u)^2$ . However only a fraction of the entries are uncorrelated and contain “new” information about the theory. The rest are primarily a measure of the noise in the experiment. Thus if we could perform a change of basis to those combinations which measure primarily signal and those which measure primarily noise we could work in a much smaller subspace of the data (the “signal” subspace) with little loss of information about the theory. In calculating the likelihood function we need to invert  $C_{ij}$ . Since matrix inversion is an  $N^3$  process, reducing the amount of data can dramatically decrease the processing time.

As a simple example of this technique, imagine that we measure a visibility twice, with independent noise in each measurement. The signal in these two measurements is totally correlated. The sum of the two measurements is primarily sensitive to the signal (with noise  $1/\sqrt{2}$  of each individual measurement) while the difference measures primarily noise. Thus if we “change basis” to the sum and difference of the two measurements we could work with the sum only with little loss of information. This would halve the size of the matrix we would need to invert in the likelihood function and speed processing by a factor  $\sim 8$ .

Optimal subspace filtering (also known as the *signal-to-noise eigenmode analysis* or *Karhunen-Loeve transform*) is a method designed to estimate the best change of basis and subspace in which to work. Recent applications of this method to the CMB and large-scale structure can be found in (Bond 1995, Bunn & Sugiyama 1995, Bunn, Scott & White 1995, White & Bunn 1995b, Bunn & White 1996, Vogeley & Szalay 1996, Bond & Jaffe 1996, Tegmark, Taylor & Heavens 1997 and Tegmark, et al. 1998). In the above example  $C_{ij} = 1$  for all  $i, j$ . This matrix has eigenvalues 2 and 0 and (orthonormal) eigenvectors  $(1, 1)/\sqrt{2}$  and  $(1, -1)/\sqrt{2}$  respectively. The eigenvalues measure the signal-to-noise carried by the combination of data points  $\vec{d} \cdot \vec{\psi}_a$ , where  $\vec{\psi}_a$  are the (orthonormal) eigenvectors.

In general it can be shown that to find the optimal subspace on which to project one finds the eigenvalues and eigenvectors of the matrix  $\sigma_i^{-1} C_{ij} \sigma_j^{-1}$  where  $\sigma_i$  is the noise<sup>7</sup> in measurement  $i$ . Since  $C_{ij}/\sigma_i \sigma_j$  is positive definite and symmetric finding the eigenvalues and eigenvectors is straightforward (e.g. by Jacobi transforms). Arrange the eigenvectors in decreasing order of eigenvalue. The first  $M$  eigenvectors in the sequence define the best  $M$ -dimensional subspace to use in filtering the noise from the data. Once increasing the dimension of the subspace adds eigenvectors whose eigenvalues are  $\ll 1$  the gain for the extra computing burden is marginal.

The advantage of optimal subspace filtering when fitting mosaiced data is obvious. One wishes to cover the  $u - v$  plane fully with the small effective apertures  $\tilde{A}$  obtained after summing the individual pointings. Thus each pointing oversamples the  $u - v$  plane considerably in terms of its larger “unmosaiced”  $\tilde{A}$ , and these visibilities are highly correlated. The optimal subspace filter identifies which combinations of the visibilities

---

<sup>7</sup>If the noise is not diagonal then the appropriate matrix is  $N^{-1/2} C N^{-1/2}$  where  $N^{1/2}$  is any square root of the noise correlation matrix, for example that defined by Cholesky decomposition.

measure primarily the cosmological signal and which are mostly noise, allowing an optimal weighting to be given to the individual visibilities sets while retaining the processing time advantage of a smaller data set.

## 7. Imaging the Microwave Sky

In addition to power spectrum estimation and parameter constraints, one goal of DASI and CBI is to image the microwave sky. Since interferometers don't measure the temperature of the CMB sky directly, it is necessary to "invert" the measured visibilities to form a sky image. In general this inversion is not unique (the DC level for example remains unconstrained) and so must be regularized. On a field-by-field basis images of the sky can be made using the usual methods of synthesis imaging in radio astronomy (e.g. Cornwell 1989) and will form a useful data checking tool.

It is possible however to try to make a larger scale image of the microwave sky using other (statistical) techniques. On degree angular scales, such as probed by DASI, regularized images have been made from the ACME/MAX (White & Bunn 1995a), Saskatoon (Tegmark et al. 1997) and CAT (Jones 1996) experiments by a variety of techniques.

Perhaps the most straightforward procedure for going from the visibility data to a sky image is Wiener filtering. Wiener filtering has been used extensively on CMB and large-scale structure data in the past (e.g. Lahav et al. 1994, Bunn et al. 1994, Zaroubi et al. 1995, Bunn, Hoffman & Silk 1996) and the reader is referred to those papers for a description of the underlying theory. The implementation of the Wiener filter in the basis defined in §6.2 is treated in many of the references given in that section.

The Wiener filter provides an estimate of the sky temperature at a point as a linear combination of the visibility data. If we assume that foregrounds and point sources have been removed from the visibility data and that the underlying sky is gaussian, then Wiener filtering is the "optimal" imaging method. Because it is linear, under the assumption of a gaussian sky, the error matrix in the map is also easy to calculate.

To proceed, let us imagine pixelizing the sky into very many small pixels at position  $\mathbf{x}_\alpha$ ,  $\alpha = 1 \cdots N_{\text{pix}}$ . This is purely a bookkeeping device which allows us to use a matrix notation for the Wiener filter, the continuum limit is obtained trivially with a sum over pixels replaced by an integral. We denote the underlying temperature fluctuation on the sky by  $t_\alpha$  which is related to the  $j$ th visibility by  $V_j = W_{j\alpha} t_\alpha + n_j$  where the weight matrix  $W_{j\alpha}$  is (see Eq. 2)

$$W_{j\alpha} = e^{2\pi i \mathbf{u}_j \cdot \mathbf{x}_\alpha} A_j(\mathbf{x}_\alpha) \quad (32)$$

and  $n_j$  is the noise in the  $j$ th visibility. We have labelled  $A_j(\mathbf{x})$  with a subscript  $j$  to allow for the possibility of mosaicing.

On an algorithmic note, it is computationally simpler to split the visibility into its real and imaginary parts and modify  $W_{j\alpha}$  to have cosine and sine components so that one deals only with real variables. The number of data points is then doubled, and the noise covariance matrix must be modified by a factor of 2 also. We shall use a complex notation, with the understanding that the implementation of the algorithm may be in terms of real valued data.

If we assume that the correlation matrices of the theory and noise are known (or computed from the data, see Seljak 1997b) then the Wiener filtered estimate of the  $t_\alpha$  is

$$t_\alpha^{WF} = C_{\alpha\beta}^S W_{j\beta} (W_{j\gamma} C_{\gamma\epsilon}^S W_{k\epsilon} + C_{jk}^N)^{-1} V_k \quad (33)$$

where  $C^S$  and  $C^N$  are the signal (Eq. 6) and noise (Eq. 16) correlation matrices. The combination  $W \cdot C^S \cdot W^T$



is essentially  $C^V$  of Eq. (12), we have written it in this way to allow the possibility of including other data sets as discussed below. Notice that the form of the Wiener filter is “signal/(signal+noise)” as is usually the case.

An expression similar to Eq. (33) can be obtained for the (formal) error correlation matrix of the estimates (see the above references). The most serious problem is that the Wiener filtered image constructed in this manner is missing large scale power. This can be included by fitting to another data set, which retains the long wavelength modes, at the same time as the visibility data. In this case one extends the data vector  $V_j$  to include the extra temperature data, with the associated  $W_{j\alpha}$ . In the case of a mapping experiment,  $W_{j\alpha}$  is simply the beam. For most current degree scale experiments it is a beam modulated on the sky by a chopping pattern. We will defer a detailed analysis of how well we can reconstruct the sky under various observing strategies, and the noise properties of the images, to a future publication where we also plan to discuss the effect of sky curvature.

## 8. Polarization

Neither the DASI or CBI will be polarization sensitive initially, however some instruments operating at smaller angular scales (e.g. the VLA) are already sensitive to linear polarization. The (linear) polarization of the CMB anisotropies is an important theoretical prediction, and can encode a great deal of information about the model (for a recent review see Hu & White 1997a) so we discuss it briefly here. Our analysis is very similar to the small-angle formalism developed in Seljak (1997a), though we caution the reader that we have a different sign convention for the  $E$ - and  $B$ -modes, see e.g. HSWZ.

We consider here only the small scale limit, so we treat the sky as a plane with a righthanded coordinate system upon it so that the sky is the  $x - y$  plane. We define polarization in the horizontal ( $\hat{x}$ ) and vertical ( $\hat{y}$ ) directions to be  $Q > 0$  and  $Q < 0$  respectively. Polarization in the  $\hat{x} + \hat{y}$  and  $\hat{x} - \hat{y}$  directions is defined to be  $U > 0$  and  $U < 0$  respectively. In terms of light traveling to us along  $\hat{z}$  the intensity tensor  $I_{ij}$ , with  $i, j = x, y$ , is

$$I_{ij} \propto \langle E_i^* E_j \rangle \propto T \mathbf{1} + Q \sigma_3 + U \sigma_1 \quad (34)$$

where the angled brackets indicate an average over a time long compared with the frequency of the wave,  $E_i$  is the electric field component and  $\sigma_k$  are the Pauli matrices. We have neglected  $V \sigma_2$  since this corresponds to circular polarization, which is not generated cosmologically. Under a rotation by an angle  $\psi$  around  $\hat{z}$  the temperature is clearly left invariant while  $Q \pm iU$  transforms as a spin-2 tensor

$$(Q \pm iU) \rightarrow e^{\mp 2i\psi} (Q \pm iU) \quad . \quad (35)$$

We expand  $Q \pm iU$  in basis states known as spin-spherical harmonics  ${}_{\pm 2}Y_{\ell m}$  with coefficients  $a_{\ell m}^{\pm 2}$  in analogy with the temperature fluctuations (Seljak & Zaldarriaga 1997; Kamionkowski, Kosowsky & Stebbins 1997; Hu & White 1997b). We can form states of definite parity,  $a_{\ell m}^{+2} \pm a_{\ell m}^{-2}$ , which are called  $E$ - and  $B$ -mode polarization respectively (not to be confused with the  $E$  and  $B$  modes of the radiation) and which have angular power spectra  $C_\ell^E$  and  $C_\ell^B$  like the temperature. In addition the  $E$ -mode of the polarization is correlated with the temperature, so there is a fourth power spectrum:  $C_\ell^{TE}$ .

The spin-2 spherical harmonics are better known in the context of quantum mechanics as Wigner functions:

$${}_s Y_{\ell m} \propto \mathcal{D}_{-s, m}^\ell = \langle \ell, -s | \mathcal{R} | \ell, m \rangle \quad (36)$$

where  $\mathcal{R} = \exp[i\vec{\alpha} \cdot \vec{J}]$  is the rotation operator and  $\vec{J}$  are the angular momentum operators. The case  $s = 0$  are the well known spherical harmonics. Thus we can relate the  ${}_{\pm 2}Y_{\ell m}$  to the usual  $Y_{\ell m}$  through raising and lowering operators (Zaldarriaga & Seljak 1997). The raising and lowering operators are differential operators since differentiating  $\mathcal{R}$  with respect to its arguments inserts  $J_{\pm} \propto J_x \pm iJ_y$  inside the bracket in Eq. (36). In the flat space case the operators are trivially  $\partial_x \pm i\partial_y$ , with an overall normalization  $\ell^{-1}$  from the normalization of the angular momentum states.

Going to the flat space limit (see Appendix) and acting on the Fourier integral with  $(\partial_x \pm i\partial_y)^2$  we find that the Fourier coefficients  $E_{\mathbf{u}}$  and  $B_{\mathbf{u}}$  are related to the measured  $Q$  and  $U$  through

$$\begin{aligned} -Q(\mathbf{x}) &= \int d^2u (E_{\mathbf{u}} \cos 2\theta_u - B_{\mathbf{u}} \sin 2\theta_u) e^{2\pi i \mathbf{u} \cdot \mathbf{x}} \\ -U(\mathbf{x}) &= \int d^2u (E_{\mathbf{u}} \sin 2\theta_u + B_{\mathbf{u}} \cos 2\theta_u) e^{2\pi i \mathbf{u} \cdot \mathbf{x}} \end{aligned} \quad (37)$$

where the signs reflect the definition of  $E$  and  $B$  in (HSWZ), and come from differentiating an imaginary exponential twice. [We caution the reader that the power spectra output by the program *CMBFAST* differ in the sign of  $C_{\ell}^{TE}$  from this convention (HSWZ). Obviously  $C_{\ell}^{EE}$  and  $C_{\ell}^{BB}$  are invariant under the sign change.] If we recall that changing the sign of the polarization rotates the polarization “vector” through  $90^\circ$  we see that the  $E$ -mode has polarization always tangential in the  $u - v$  plane (Seljak 1997a; it would be radial under a sign change).

We now have 4 non-vanishing power spectra, all diagonal in  $\mathbf{u}$ , whose diagonal parts we can denote by  $S^{TT}$ ,  $S^{EE}$ ,  $S^{BB}$  and  $S^{TE}$  in analogy with Eq. (7). This is all the formalism we need to allow us to reconstruct the power spectrum of temperature and polarization, or provide constraints on theoretical models. We proceed as in Hu & White (1997a; see also Zaldarriaga 1997) by defining a vector of our data  $D_I = (T_1, Q_1, U_1; \dots; T_N, Q_N, U_N)$  at each point  $\mathbf{u}_i$ . The likelihood function for this data is analogous to Eq. (18) with a correlation matrix

$$C_{IJ}^{XY} \propto \int d^2u \tilde{A}_i(\mathbf{u}) \tilde{A}_j(\mathbf{u}) \sum_{\alpha, \beta} \omega^{X\alpha}(\theta_u) \omega^{Y\beta}(\theta_u) S^{\alpha\beta}(u) \quad (38)$$

where  $X, Y = (T, Q, U)$  and  $\alpha, \beta = T, E, B$  with  $\omega^{TT} = 1$ ,  $\omega^{QE} = -\cos 2\theta$ ,  $\omega^{QB} = \sin 2\theta$ ,  $\omega^{UE} = -\sin 2\theta$ ,  $\omega^{UB} = \cos 2\theta$ .

Given a set of measurements one can reconstruct the power spectrum of the temperature or the polarization as described in §5.2. Alternatively one can provide upper limits (or measurements) of a bandpower for polarization or temperature by calculating  $\mathcal{L}(Q^2)$  where  $Q^2$  is the amplitude of a flat power spectrum (i.e.  $\ell(\ell + 1)C_{\ell} = \text{constant}$ ) for the  $TT$ ,  $TE$ ,  $EE$  and  $BB$  power spectra. [If information on the temperature is absent one merely drops the  $X = T$  entries of the correlation matrix above.] If one believes that there is no foreground contamination, the cosmological signal on small scales should be dominated by  $E$ -mode polarization and so one can set  $Q_B = 0$  in evaluating the likelihood.

## 9. Discussion

The theoretical study of CMB anisotropies has advanced considerably in recent years, both in terms of theoretical predictions and comparison with observational data. In this paper we have developed some of the formalism necessary for the analysis of interferometer data, such as will be returned by VSA, DASI, CBI and VLA, in the modern language of anisotropy (temperature and polarization) power spectra. Although the

fundamental entities measured by an interferometer differ considerably from those measured in single-dish experiments, much of the analysis can be presented in an analogous manner including power spectra, window functions and the like. This allows one to use directly the sophisticated analysis techniques which already exist for single-dish experiments.

The formalism presented here is based upon the “flat sky” approximation and is thus best suited to the study of small-scale anisotropies. In this regime interferometers can provide high-sensitivity measurements of the high- $\ell$  peaks in the angular power spectrum, effects of gravitational lensing, the damping tail of the anisotropies and proto-galaxy formation and second order anisotropies. For CBI the cosmological signal would be higher if the universe had significant spatial curvature since this would shift the features in the angular power spectra to smaller angular scales, however for both VSA and DASI significant signal is expected simply based on existing measurements.

Several outstanding problems remain, all associated with extending the framework of this paper to larger angular scales where the curvature of the sky and the full 3D nature of the Fourier Transforms become important. We intend to return to these issues in a future paper.

We would like to acknowledge useful conversations with Wayne Hu, Douglas Scott and Max Tegmark. We thank Lyman Page for many comments which helped to clarify the paper. M.W. thanks Pedro Ferreira for conversations during the initial phases of this work.

### A. Flat Sky Approximation

The derivation of the correlation function Eq. (7) given in the text is sufficient for the purposes of this paper. However, sometimes it is convenient to treat the sky as flat and replace spherical harmonic sums with Fourier Transforms at the temperature (rather than the 2-point function) level. We give some details of this in this Appendix, the reader is also referred to Zaldarriaga & Seljak (1997).

In the flat sky approximation we replace the spherical polar coordinates  $(\theta, \phi)$  by radial coordinates on a plane:  $r \equiv 2 \sin \theta/2 \approx \theta$  and  $\phi$ . We can exchange our indices  $(\ell, m)$  for a 2D vector  $\mathbf{l}$  with length  $\ell$  and azimuthal angle  $\varphi_\ell$  and define

$$a(\mathbf{l}) \equiv \sqrt{\frac{4\pi}{2\ell+1}} \sum_m i^{-m} a_{\ell m} e^{im\varphi_\ell} \quad (\text{A1})$$

with  $a(-\mathbf{l}) = a^*(\mathbf{l})$ . We now expand our temperature field in terms of multipole moments as usual with

$$\sum_{\ell m} a_{\ell m} Y_{\ell m} = \frac{1}{2\pi} \int d\ell d\varphi_\ell a(\mathbf{l}) \sqrt{\frac{2\ell+1}{4\pi}} \sum_m i^m e^{-im\varphi_\ell} Y_{\ell m} \quad (\text{A2})$$

where we have replaced the sum over  $\ell$  with an integral.

Writing the sum over  $m$  in terms of  $m < 0$  and replacing the associated Legendre polynomials with Bessel functions using Gradshteyn & Ryzhik (1980; Eq. 8722(2)) we have

$$\sum_{\ell m} a_{\ell m} Y_{\ell m} \approx \frac{1}{(2\pi)^2} \int d\ell d\varphi_\ell a(\mathbf{l}) \left[ J_0(\ell\theta) + 2 \sum_{m=1}^{\infty} i^m J_m(\ell\theta) \cos m(\phi - \varphi_\ell) \right] . \quad (\text{A3})$$

The term in square brackets is simply the Rayleigh expansion of a plane wave so we finally obtain, writing  $\mathbf{l} = 2\pi\mathbf{u}$ ,

$$\frac{\Delta T}{T}(\mathbf{x}) = \sum_{\ell m} a_{\ell m} Y_{\ell m} \approx \int d^2 u a(\mathbf{u}) \exp[2\pi i \mathbf{u} \cdot \mathbf{x}] \quad (\text{A4})$$

and of course the two point function for  $a(\mathbf{u})$  is diagonal:

$$\langle a^*(\mathbf{u})a(\mathbf{w}) \rangle = C_{\ell} \delta^{(2)}(\mathbf{u} - \mathbf{w}) \quad . \quad (\text{A5})$$

These expressions can then be used to derive Eq. (8), though the derivation presented above Eq. (7) uses more controlled approximations. The generalization of Eq. (A4) to polarization is presented in §8.

## REFERENCES

- Banday A., Wolfendale A.W., 1991, MNRAS, 248, 705
- Becker R.H., White R.L., Helfand, D.J., 1996, ApJ, 450, 559
- Bennett C.L., et al. 1992, ApJ, 396, L7
- Bennett C.L., Turner M., White M., 1997, Physics Today, November, 32
- Bond J.R. 1995, Phys. Rev. Lett., 74, 4369.
- Bond J.R., Efstathiou G., Tegmark M., 1997, MNRAS, 291, L31
- Bond J.R., Jaffe, A.H., 1996, in “Microwave Background Anisotropies”, Proceedings of the XVIth Moriond Meeting, ed. F. Bouchet et al., p.197 [astro-ph/9610091]
- Bond, J.R., Jaffe, A.H., Knox, L., 1998, Phys. Rev. D57, 2117
- Brandt, W.N., Lawrence, C.R., Readhead, A.C.S., Pakianathan, J.N., Fiola, T.M., 1994, ApJ, 424, 1
- Bunn, E.F. 1995, Ph.D. thesis, University of California, Berkeley.
- Bunn, E.F., et al., 1994, ApJ, 432, L75
- Bunn, E.F., Hoffman, Y., Silk, J., 1996, ApJ, 464, 1
- Bunn, E.F., Scott D., & White M. 1995, ApJ, 441, L9.
- Bunn, E. F. & Sugiyama, N. 1995, ApJ, 446, 49.
- Bunn, E. F. & White, M. 1996, ApJ, 480, 6
- Cornwell, T., 1989, “Synthesis Imaging in Radio Astronomy”, ASP conference series vol 6, ed. R. Perley, F. Schwab, A. Bridle, p. 277
- Church, S. E., 1995, MNRAS, 272, 551
- Dodelson, S., 1997, ApJ, 482, 577
- Draine, B.T., Lazarian, A., 1998, ApJ, 494, L19

- Fixsen D.J., et al., 1996, ApJ, 473, 576
- Franceschini, A., et al., 1991, A&AS, 89, 285
- Gorski K.M., Banday A.J., Bennett C.L., Hinshaw G., Kogut A., Smoot G.F., Wright E.L., 1996, ApJ464, L11
- Gradshteyn, I.S., Ryzhik, I.M., 1980, “Table of Integrals, Series and Products” (Academic Press, New York)
- Hobson, M.P., Lasenby, A.N., Jones, M., 1995, MNRAS, 275, 863
- Hobson, M.P., Magueijo, J., 1996, MNRAS, 283, 1133
- Hu, W., White, M., 1997a, New Astronomy, 2, 323
- Hu, W., White, M., 1997b, Phys. Rev. D56, 596
- Hu, W., Seljak, U., White, M., Zaldarriaga, M., 1998, Phys. Rev. D57, 3290
- Jones, M.E., 1996, in “Microwave Background Anisotropies”, Proceedings of the XVIth Moriond Astrophysics Meeting, Les Arcs, France, ed. F.R. Bouchet et al., p.161 [astro-ph/9611212]
- Jungman G., Kamionkowski M., Kosowsky A., Spergel D.N., 1996, Phys. Rev. D48, 3502
- Kamionkowski, M., Kosowsky, A., Stebbins, A., 1997, Phys. Rev. Lett. 78, 2058
- Kogut, A., 1997, AJ, 114, 1127
- Kogut, A., Hinshaw, G., Banday, A.J., Bennett, C.L., Gorski, K., Smoot, G.F., Wright, E.L., 1996, ApJ, 464, L5
- Lahav, O., Fisher, K.B., Hoffman, Y., Scharf, C.A., Zaroubi, S., 1994, ApJ, 423, L93
- Lawson K.D., et al., 1987, MNRAS, 225, 307
- Leitch, E.M., Readhead, A.C.S., Pearson, T.J., Myers, S.T., 1997, ApJ, 486, L23
- Martin, H.M., Patridge, R.B., 1988, ApJ, 324, 794
- de Oliveira-Costa, A., Kogut, A., Devlin, M.J., Netterfield, C.B., Page, L.A., Wollack, E.J., 1997, ApJ, 482, L17
- Nordberg H.P., Smoot G., 1998, preprint [astro-ph/9805123]
- O’Sullivan C., et al., 1995, MNRAS, 274, 861
- Peacock, J.A., Nicholson, S.F., 1991, MNRAS, 253, 307
- Platania, P., et al., 1998, preprint [astro-ph/9707252]
- Popieszalski, M.W., Proc. of 23rd European Microwave Conference, Madrid, Spain September 1993, p. 73
- Reynolds, R.J., 1992, ApJ, 392, L35
- Scott D., White M., 1995, Gen. Rel. & Gravitation, 27, 1023
- Schlegel, D.J., Finkbeiner, D.P., Davis, M., 1998, ApJ, in press [astro-ph/9710327]

- Seljak, U., 1997a, ApJ, 482, 6
- Seljak, U., 1997b, preprint [astro-ph/9710269]
- Seljak, U., Zaldarriaga, M., Phys. Rev. Lett. 78, 2054
- Smoot, G., Scott, D., 1997, Review of Particle Properties, Ch.20 [astro-ph/9711069]
- Stompor R., Efstathiou G., 1998, preprint [astro-ph/9805294]
- Subrahmanyan, R., Ekers, R.D., Sinclair, M., Silk, J., 1993, MNRAS, 263, 416
- Tegmark, M., 1997a, preprint [astro-ph/9712038]
- Tegmark, M., 1997b, Phys. Rev. D55, 5895
- Tegmark, M., Efstathiou, G., 1996, MNRAS, 281, 1297
- Tegmark, M., et al. 1997, ApJ, 474, L77
- Tegmark, M., et al., 1998, ApJ, 499, 555
- Tegmark, M., Taylor, A.N., Heavens, A.F., 1997, ApJ, 480, 22
- Toffolatti, L., et al., 1994, Astrophys. Lett. & Comm., in press [astro-ph/9410037]
- Toffolatti, L., et al., 1997, preprint [astro-ph/9711085]
- Tompson A.R., Moran J.M., Swenson G.W., 1986, “Interferometry and Synthesis in Radio Astronomy”  
(New York: Wiley)
- Vogeley, M. S. & Szalay, A. S. 1996, ApJ, 465, 34.
- White M., 1998, Phys. Rev. D57, 5273
- White, M., Bunn, E.F. 1995a, ApJ, 443, L53
- White, M., Bunn, E.F. 1995b, ApJ, 450, 477; erratum 460, 1071
- Wright, E.L., 1998, ApJ, 496, 1
- Zaldarriaga, M., Seljak, U., 1997, Phys. Rev. D55, 1830
- Zaldarriaga M., Spergel D.N., Seljak U., 1997, ApJ, 488, 1
- Zaldarriaga, M., 1997, preprint [astro-ph/9709271]
- Zaroubi, S., Hoffman, Y., Fisher, K.B., Lahav, O., 1995, ApJ, 457, 50

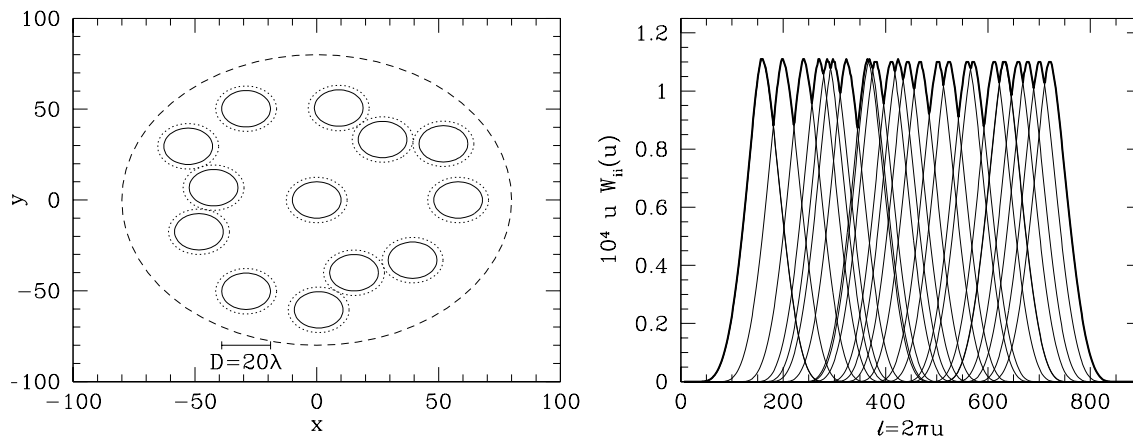


Fig. 1.— (a) The physical configuration of the DASI receivers. The axes are graduated in wavelengths, physical separations are obtained by multiplying by  $\lambda = 1$  cm. Each dish has an effective optical diameter  $D = 20\lambda$  (solid lines). The physical size of the dishes is 25cm (dotted lines) and the base plate for DASI is 1.6m in diameter (dashed line). Correlations are measured between all pairs of horns, so the instrument samples 78 baselines. Note the 3-fold symmetry of the array, which means that 26 different  $u$ 's are sampled. (b) The sensitivity of DASI vs  $\ell = 2\pi u$  for the configuration in (a). The window functions are shown for each of the 26 different  $u$ 's sampled, and the bold line traces the outline of these 26 window functions.

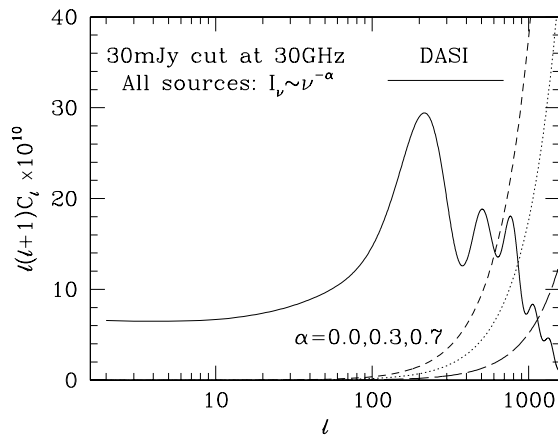


Fig. 2.— The angular power spectrum of the standard CDM model (solid) in dimensionless units. The horizontal line represents the range of angular scales probed by DASI. The dashed and dotted lines are the angular power spectrum of fluctuations from unresolved point sources. These have been modeled by taking the luminosity function of VLA FIRST (Becker et al. 1996) radio sources at 1.5 GHz as provided by Tegmark & Efstathiou (1996; Eq. 43) and extrapolating *all* sources to 30 GHz using  $I_\nu \sim \nu^{-\alpha}$  with  $\alpha = 0, 0.3, 0.7$ . All sources brighter than 30mJy at 30 GHz have been removed.

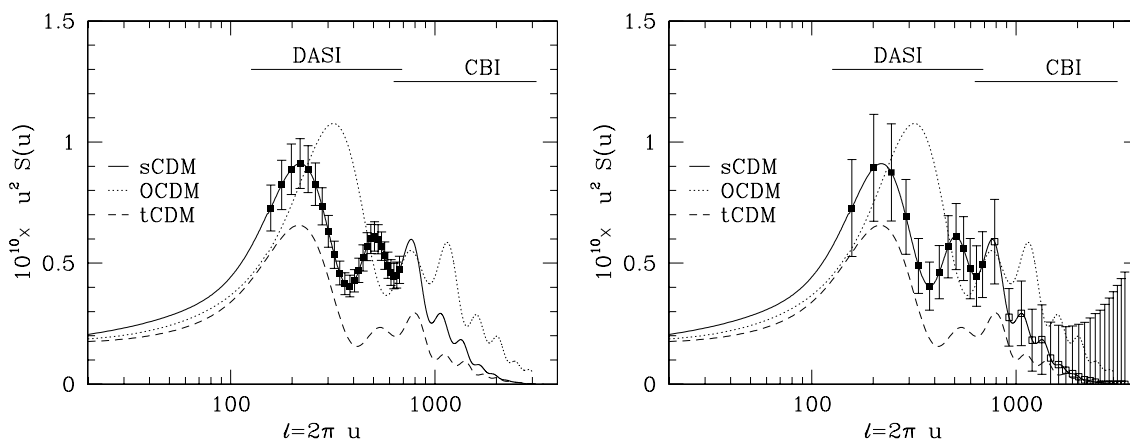


Fig. 3.— The 2D power spectrum per logarithmic interval in  $u$ , for a selection of COBE normalized models chosen to provide good fits to the large-scale structure data (see text). The solid lines across the top of the plot illustrate the range of scales to which DASI and CBI will be sensitive. The left panel shows the expected uncertainties per bin for the sCDM model for 1 month of observing of 25 widely separated points on the sky. For display purposes we have placed the points on the sCDM curve. Each of the 26 baselines is shown and the signal-to-noise is about 1 in the highest- $u$  bin. Though each baseline has independent receiver noise, the window functions for neighboring points overlap considerably so the cosmological signal is very correlated between points. The right panel shows the result with 6 months of integration using a mosaicing strategy covering  $\sim 400$  square degrees of sky (again with  $S/N \sim 1$  in the final bin). In this case each of these points is completely independent. We have also shown the expected error bars for CBI, assuming a similar mosaicing strategy.



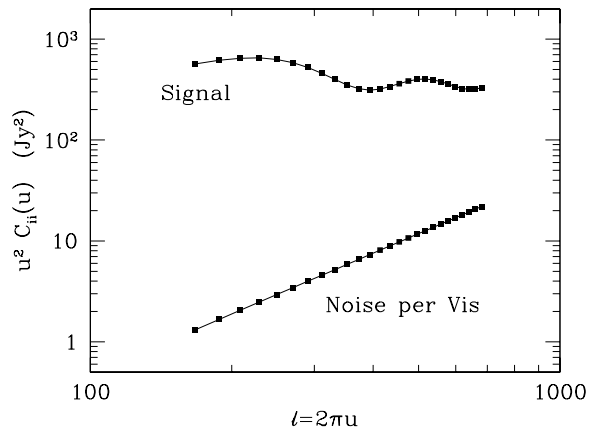


Fig. 4.— The 26 diagonal elements of the correlation matrix  $C_{ii}^V$  and  $C_{ii}^N$  for *COBE* normalized  $\Lambda$ CDM and a pillbox aperture function. The noise is assuming 1 day of operation of DASI and is per visibility. We have shown results for 1 pointing, without the instrument rotation necessary to fill the  $u-v$  plane. The signal in each of these visibilities will be highly correlated due to strongly overlapping window functions (see text).

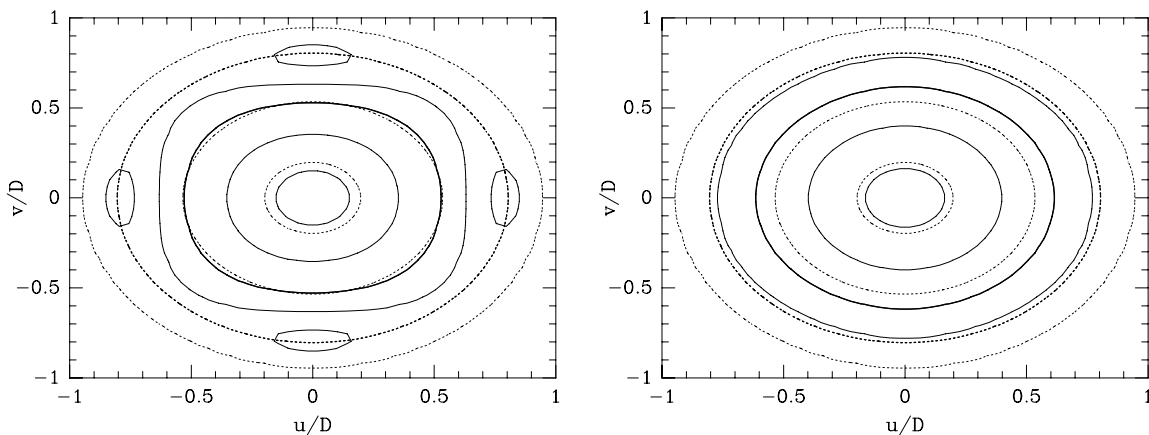


Fig. 5.— The aperture function  $|A(\vec{u})|^2$  for (a)  $3 \times 3$  square mosaic with spacing  $D/2$  (b) 7 points laid out in 3 rows (at the center and vertices of a regular hexagon) with all neighbors separated by  $D/2$ . Contours mark 1, 2, 3 and  $4\sigma$  from the peak with  $3\sigma$  shown thick ( $1\sigma = e^{-1/2}$  of peak power). The dashed lines indicate the unmosaiced aperture of the primary beam, the solid lines the result after mosaicing.